"Illuminating" electron diffusion regions of collisionless magnetic reconnection using electron agyrotropy

Jack Scudder[1] and William Daughton[1,2]

Received 14 January 2008; revised 15 April 2008; accepted 24 April 2008; published 28 June 2008.

[1] Agyrotropy is a scalar measure of the departure of the pressure tensor from cylindrical symmetry about the local magnetic field direction. Ordinarily electrons are well modeled as gyrotropic with very small agyrotropy. Intensified layers of electron agyrotropy are demonstrated to highlight the thin electron gyroradius scale boundary regions adjoining separatrices, X and O lines of full particle simulations of collisionless magnetic reconnection. Examples are presented to show these effects in antiparallel and guide field geometries, pair plasmas, and simulations at a variety of mass ratios, including a hydrogen plasma. Agyrotropy has been determined from the PIC pressure tensor using a new, fast algorithm developed to correct discreteness contributions to the apparent agyrotropy. As a local scalar diagnostic, agyrotropy is shown to be potentially useful with single spacecraft data to identify the crossing or proximity of electron scale current layers, thus providing a kinetic level diagnosis of a given layer's ability to be a possible site of the collisionless reconnection process. Such kinetic tools are certainly complimentary to the other macroscopic signatures of reconnection. Because of the extreme circumstances required for electron agyrotropy, detection of these signatures with framing macroscopic signatures might prove useful for the discovery of new reconnection sites in nature and 3-D codes of collisionless reconnection. The agyrotropy in the 2-D PIC codes reflect long-lived bulges on the distribution function that appear to be organized by the direction and size of slowly evolving perpendicular electric fields in these layers and are not consistent with gyrophase bunching.

Citation: Scudder, J., and W. Daughton (2008), ''Illuminating'' electron diffusion regions of collisionless magnetic reconnection using electron agyrotropy, *J. Geophys. Res.*, *113*, A06222, doi:10.1029/2008JA013035.

1. Introduction

[2] In situ evidence of the occurrence of collisionless magnetic reconnection (CMR) in space plasmas was initially provided by corollaries of CMR in macroscopic variables, such as flows and magnetic components that were external to the reconnection layer proper. Pioneering attempts in this vein were made by *Paschmann et al.* [1979] and *Sonnerup et al.* [1981], who identified accelerations of the *Walen* [1944] type, certifying rotational discontinuities embedded in the magnetopause current layer, a corollary to the presence of a normal component of **B** at the magnetopause. Recently the experimental focus has shifted toward finding the kinetic signatures of CMR at work [*Scudder et al.*, 2002; *Mozer*, 2005], specifically those signatures of the innermost "Electron Diffusion Region" (EDR). Recent results from large scale kinetic simulations [*Daughton et al.*, 2006; *Karimabadi et al.*, 2007; *Shay et al.*, 2007] as well as space observations [*Phan et al.*, 2007] suggest that the length of the EDR may be much larger than previously thought [*Shay et al.*, 2001; *Hesse et al.*, 1999]. As a consequence, these highly elongated electron layers may play an important role in determining the time dependence and macroscopic evolution of the reconnection process. These recent developments point to the need for new observational techniques to better identify and characterize the EDR in magnetospheric plasmas. This shift of focus requires better spatial (temporal) resolution and new tools for finding and identifying these very narrow layers (2–10 km at the forward magnetopause). While the Walen style acceleration corollaries of reconnection remain important to the context of certifying large scale consequences of reconnection layers, there is an increasing awareness that the Walen signatures by themselves are not conclusive in the absence of identifying the associated EDR.

[3] With this change in focus there are new observational challenges that are also theoretical ones. Where in the CMR layer were the measurements acquired? This in turn requires an agreed upon set of properties of each of these layers; at present this is not a completed process. In the interim, various ad hoc "properties" have been used to chart, if not define, the observer's path [*Mozer*, 2005]. Immersion in the ion diffusion region is conflicted by the simulations that report no generic "expected" Hall pattern [*Rogers et al.*, 2001]. Even depressions of B do not qualify for passing through a diffusion region! [e.g., *Lemaire and Burlaga*, 1976]. New empirical sieves with strong theoretical foun-

[1]Department of Physics and Astronomy, University of Iowa, Iowa City, Iowa, USA.
[2]Los Alamos National Laboratory, Los Alamos, New Mexico, USA.

0148-0227/08/2008JA013035

dations are required to screen identified current sheets for their convincing relevance as an EDR enabling site for reconnection. Since the electrons are locally disrupted in the EDR, the screen for being in the electron diffusion region should, if at all possible, be electron specific, not just a compressible magneto-hydrodynamic corollary (such as there must be a parallel E) that could be confused with less radical explanations. A significant difficulty for the confident location of the EDR is that the properties of the EDR have not been established by analytic theory, jump conditions, or numerical solution of MHD or Hybrid models of the reconnection layer, since all these models suffer from the unknown closure equations for the plasma [*Scudder*, 1997]. This paper is an approach to this problem of labeling and finding EDR layers using a new tool, the electron agyrotropy $A\emptyset_e$, a broken symmetry of the electron pressure tensor that indexes local demagnetization of the electrons.

[4] Fully kinetic PIC simulations of reconnection layers possess the generality necessary to benchmark self-consistent observables of reconnection layers and hence, traversal of the EDR. Such simulations (i) possess a global overview of all the parts of the electrodynamics at a given time, (ii) permit a record of all spatial and velocity space observables and relatives (vector potential, electrical potential, and species streamlines) that are essential to understanding the evolving dynamics, and (iii) are at present the only self-consistent theoretical model of CMR that breaks the frozen flux condition in a model independent way, forgoing ad hoc equations of state and ad hoc resistivity models that limit the generality of the prediction of MHD, two-fluid, or hybrid treatments.

[5] In this paper (i) we introduce theoretical and computational arguments that the agyrotropy $A\emptyset_e$ of the electron pressure tensor (its departure from cylindrical symmetry about the local magnetic field direction) is in principle, a presently measurable scalar diagnostic of EDRs both for PIC simulations and space plasma instruments, that capably differentiates X and O point topologies. We also (ii) analyze the ''forward'' problem of the occurrence and relation of agyrotropy enhancements to their known separatrices and separators of their CMR layers determined by flux surfaces from the vector potential within a variety of 2-D PIC simulations. In this way we seek to motivate the use of agyrotropy as a (single spacecraft) marker for electron gyroradius scale layers that are prerequisite to electron gyroviscous support of the reconnection electric field. We also have sketched the difficulties for such measurements that arise from aliasing and other consideration. It would appear that this argument (a) can be transferred into 3D simulations to locate EDRs (since no flux labeling is possible there from the vector potential) and (b) to aid the ''inverse'' problem of finding and screening candidate current layers in spacecraft data as Electron Diffusion Regions (EDRs), especially when magnetic nulls are not intercepted.

[6] The paper is comprised of seven sections**:** Definition of $A\emptyset_e$ and Its Association With Collisionless Magnetic Reconnection (CMR); If Agyrotropy Were Observable, What Could Be Seen?; Agyrotropy Is Presently Detectable; Agyrotropy Determinations From PIC Simulations; Recovery of Analytic Results for $A\emptyset$ of *Harris* [1962] Equilibrium With Background; Associating Agyrotropy and Toplogical Boundaries; and Summary and Discussion.

2. Definition of $A\emptyset_e$ and Its Association With Collisionless Magnetic Reconnection (CMR)

[7] The pressure tensors of the plasma $\overleftrightarrow{\mathbf{P}}_j$ contain the velocity space average of the stresses that result from all guiding center drifts and finite Larmor radius (FLR) effects [*Parker*, 1957]. *Vasyliunas*'s [1975] review argued persuasively that steady CMR in 2-D was only possible with the assistance of momentum transfers implied by steady spatial gradients of the electron pressure tensor $\underline{\mathbf{P}}_e$ (**x**); further, he argued that these effects could only occur when $\underline{\mathbf{P}}_e$ (**x**) was agyrotropic $A\emptyset_e \neq 0$, in the vicinity of the null point. This argument does not say how the tensor becomes demagnetized, but does require a time independent non-gyrotropic pressure tensor. Recent kinetic 2-D PIC simulations for this and other geometries have tended to reinforce this theoretical argument, showing that the ''electron-gyroviscous'' effect made possible by the divergence of the electron pressure tensor was the principal supporting term for the reconnection electric field at the separator [*Hesse et al.*, 1995; *Kuznetsova et al.*, 1998; *Pritchett*, 2001; *Ricci et al.*, 2004; *Daughton et al.*, 2006; *Karimabadi et al.*, 2007]. However, there remains the logical possibility that other terms in the time averaged generalized Ohm's law, loosely referred to as ''anomalous resistivity'' effects, might play an unforeseen role, either away from the separator in 2-D layers, or be permitted in 3-D current layers where new **k** are possible [e.g., *Drake et al.*, 2002]. Although 3-D simulations of reconnection are in their infancy, the limited information from them indicates the persistence in 3-D of the 2-D effects of the pressure tensor. The present paper focuses on diagnostics for the already identified ''electron-gyroviscous'' contributions to the reconnection electric field and finding ways to locate regions narrow enough to play such a role.

[8] Throughout this paper, we adopt the traditional definition for a species to be magnetized: the typical gyroradius R_j, of the j'th species with perpendicular random velocity $\mathbf{w}_{\perp j}$ and bulk velocity $\mathbf{U}_{\perp j}$ (determined by the average perpendicular speed $\langle v_{\perp j}\rangle = \langle|\mathbf{U}_{\perp j} + \mathbf{w}_{\perp j}|\rangle$ and the condition $R_j = \langle v_{\perp j}\rangle/\Omega_{cj}$, where the denominator is the species cyclotron frequency), should be small compared to the scale of the spatial variations of forces encountered, L, viz $R_j/\mathrm{L} \ll 1$; in addition it is required that the external and explicit time dependence experienced is slow compared to its gyro frequency [*Rossi and Olbert*, 1970; *Hasegawa*, 1975; *Golant et al.*, 1980; *Hazeltine and Waelbroeck*, 1998; *Bellan*, 2006]. In the subthermal flow regimes $R \rightarrow \rho$, the thermal gyroradius, while in superthermal flow $R_j \rightarrow U_{\perp j}/\Omega_{cj}$, the convected inertial length often used in collisionless shocks. This approximation is known variously as the Alfven approximation, the adiabatic approximation, the guiding center approximation, or even the drift kinetic approximation; it is usually invoked for plasmas where the magnetic field is strong, allowing the velocity distribution function to be well modeled in its rest frame as a function of parallel velocity and perpendicular speed:$f(v_{\|}, v_{\perp})$, and the pressure tensor to be simplified to a field aligned diagonal

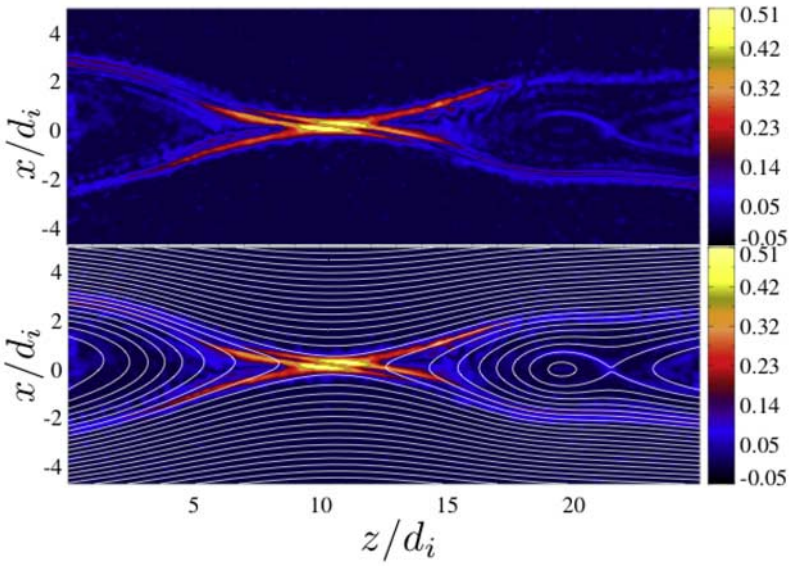

Figure 1. Spatial variation of electron agyrotropy $A\emptyset_e$ (x, y, $t\,\Omega_{ci} = 43$) during evolution of a perturbed Harris sheet with 30% background density, a guide field 50% that of the reconnecting field, $m_i/m_e = 25$, $T_i/T_e = 5$, and $\omega_{pe}/\Omega_{ce} = 3$ at $t\Omega_{ci} = 43.4$. (top) Color coded spatial variation of $A\emptyset_e$; (bottom) $A\emptyset_e$ from the upper panel with superposed white curves that locate mathematically exact magnetic flux surfaces from the vector potential. Attention is drawn to the pattern of nonzero $A\emptyset_e$ that presages the location of the flux separatrices and highlights the X point and the other topological structures of B in formation.

representation with two equal eigenvalues transverse to the magnetic field.

[9] The opposite regime where electron are demagnetized is reflected in nonzero $A\emptyset_e$, defined as the absolute value of the difference divided by the average of the two pressure eigenvalues associated with eigenvectors perpendicular to the mean magnetic field direction:

$$A\emptyset_e = 2\frac{|P_{\perp e1} - P_{\perp e2}|}{P_{\perp e1} + P_{\perp e2}}. \quad (1)$$

Gyrotropic plasmas, presumed in the drift kinetic equation, have $A\emptyset \equiv 0$; agyrotropy is bounded from above by the extreme value of 2. An explicit technique for isolating the two perpendicular eigenvalues of the pressure tensor, even when it is agyrotropic, is fully discussed in Appendix A. In the supersonic regime (as with ions behind a shock wave) the demagnetization of the bulk flow allows a strong exchange between flow and random energies that will not initially be organized by the magnetic field direction. Accordingly the signatures of agyrotropy of the subsonic type as in 1 is sufficiently general to intercept both types of demagnetization whether the violation is one associated the convected inertial length or the gyroradius.

[10] The electron thermal gyro radius ρ_e, skin depth $d_e = c/\omega_{pe}$, and Debye length λ_{De}, are usually the three smallest scale lengths in a plasma, with ρ_e and d_e interchanging relative sizes when $\beta_{\perp e}$ passes unity. The scale L of most obstacles and gradients in astrophysical plasmas are much larger than any of these, and the electrons are justifiably modeled as magnetized. As presently theoretically understood [e.g., *Chacon et al.*, 2007], CMR layers involve magnetic gradient scales $L_B \simeq; d_e$. Since $R_e \geq \rho_e \equiv \beta_{\perp e}^{1/2} d_e$ the strongest current layers of CMR flows will involve demagnetized thermal electrons and hence electron agyrotropy, certainly in antiparallel geometries. Simulation evidence as in Figure 1 below and that of *Hesse et al.* [1999], *Pritchett* [2001], and experimental data [*Scudder and Mozer*, 2005] suggest, however, that even in the presence of guide fields that the electrons can become demagnetized, generating gyroviscous contributions to **E**. At the present point of CMR research, electron agyrotropy appears to be essential to the process of magnetic reconnection. Some ask whether it is a cause or a consequence. While this is not firmly established, a point of view can be consistently held that as current layers thin toward electro gyro scales, there comes a point when a sufficient part of the thermal electrons are all non-guiding center ordered by the short scales and the orderly labeling of flux tubes in time must be suspended. With that view the agyrotropy of the electrons is the marker of that transition. Both it and CMR are commonly facilitated by the thinning of current sheets to such a disruptive scale. From this vantage point there is neither a cause nor consequence, they attend one another. The formation of such thin scales is rare. However, there are Vlasov equilibria that possess steady state electron agyrotropy without being reconnecting layers; such layers are, however, highly unstable to tearing.

[11] Agyrotropy should, however, only rarely be expected in space plasma data, given the successes of the last 50 years

of understanding large volumes of near earth and solar system plasmas with collisionless ideal, but anisotropic (gyrotropic) MHD [cf. *Burlaga*, 1995]. The pervasive expectation of gyrotropic electrons in space plasmas is also the rationale for in flight intracalibration schemes [e.g., *Scudder et al.*, 1995]. The short scale condition for electrons that leads to nonzero $A\emptyset_e$ is almost synonymous with the non-ideal behavior expected in the EDR of the CMR layer. Accordingly, the a priori occurrence of $A\emptyset_e$ is much rarer than the incidence of accelerations of a rotational discontinuity that satisfy the Walen test. By this argument, validated detections of $A\emptyset_e$ would indicate a much closer proximity to the EDR of the CMR than the certification of Walen accelerations. The strongest experimental identification for CMR in action would be supporting signatures of demagnetization of the EDR and the surrounding, external accelerations to complete the evidence of topology change. Either diagnostic by itself is weaker than their coordinated detection. Isolated detection of relatively rare $A\emptyset_e$ should be more diagnostic of locale than isolated detection of Walen style accelerations. Hence in terms of proximity to non-ideal effects we suggest detection of both $A\emptyset_e$ and Walen accelerations as more sure, than $A\emptyset_e$ alone, with Walen accelerations detections being the least surgical identification technique when used alone.

[12] From the structure of the electron form of the frozen flux theorem [*Rossi and Olbert*, 1970] there are only two types of violations of the frozen flux theorem: those from pressure stresses (which also include ''inertial effects,'' and those associated with momentum transfer enabled by time dependence). The steady state slippage of the magnetic flux envisaged at sites of CMR occurs at gradients in current layers so steep that the thermal electrons (the bulk of the flux and pressure by number) experience non-adiabatic FLR corrections, leaving the ''fingerprint'' of this disruption in their pressure tensor, guaranteeing a nonzero $A\emptyset_e$ as demonstrated below. Since these same electrons determine the local electron fluid velocity, these disruptions also imply that the ''inertial'' terms to the generalized Ohm's law will also play a potentially dominant role in areas where the electron flows are superthermal.

3. If Agyrotropy Were Observable, What Could Be Seen?

[13] Agyrotropy is illustrated in Figures 1a and 1b as determined from a two dimensional, full PIC simulation of a reconnecting current sheet with a guide field equal to the reconnecting fields, $\omega_{pe}/\Omega_{ce} = 3$, and $m_i/m_e = 25$. An initial perturbation is employed to initiate reconnection and open boundary conditions [*Daughton et al.*, 2006] are used along all boundaries. The upper panel (Figure 1a) displays a two dimensional snapshot of the spatial variations of the electron agyrotropy $A\emptyset_e$ that is strongly enhanced in an X pattern, suggestive of a saddle point; hints occur at the right of center of the formation of a secondary X with an intermediate O type boundary. These impressions are confirmed in the lower panel where the pattern of field lines, determined mathematically by the isocontours of the vector potential A_z, have been superposed on the $A\emptyset_e$ intensity surface Even if A_z (t) were an observable, or could be locally reconstructed, it varies smoothly across the separatrices, providing no model independent way to establish the locale of the spacecraft observations. By contrast, the profile of $A\emptyset_e$ has a perceptible, structured nonzero enhancement inside the separatrices or about the separator region and then only near where a spatial organization reflects that of the flux surfaces. $A\emptyset_e$ (t) is potentially an observable from spacecraft data, the flux surfaces in 1b are not. Even the magnetic field does not give a strong indication of proximity to the separatrices. In this way we demonstrate that agyrotropy locally ''illuminates'' the locale of the separatrices and separator environs of the reconnection layer.

[14] Careful inspection shows that the layers of enhanced $A\emptyset_e$ occur on the outflow side of the separatrices, rather than precisely astride them. The local ''marker'' provided by $A\emptyset_e$ is a distinct improvement for the observer struggling to identify events as being in different non-ideal regimes of the reconnection layer. This is not a working hypothesis, but demonstrated in a nearly model free way by superposing the contours of flux surfaces on $A\emptyset_e$ (an observable from in situ plasma measurements of size demonstrated below to be detectable). Movies of the simulations also illustrate the patterns of agyrotropy evolving slowly of ion timescales. We show below (see Figure 7) that one of the two orthogonal transverse pressure eigenvectors is essentially aligned with $\mathbf{E}_\perp$ when $A\emptyset_e \neq 0$; it is also known that the pattern of $\mathbf{E}_\perp$ evolves on the ion timescale. From these facts we conclude that the agyrotropic bulge pattern on f_e $(\mathbf{v})$ must be maintained at or 0° or 90° to the direction of $\hat{\mathbf{E}}_\perp$, rather than possibly precessing as a gyrophase bunched group of electrons.

[15] $A\emptyset_e$ is strongest at the principal X separator of Figure 1a, but contiguous regions along the separatrices are also illuminated and appear to be a spatially structured extensions of the same agyrotropic layer of reduced size. The demagnetization ($A\emptyset_e > 0$) has different levels throughout a region that starts at the separator but extends on ion scales - not only along the horizontal electron exhausts jets [*Daughton et al.*, 2006; *Karimabadi et al.*, 2007], but also out along the separatrices which are the probable locale of most of the DEFE events reported by *Scudder and Mozer* [2005]. This demagnetized region is a non-convex region with curved ''arms'' emanating from a more convex highly elongated rectangular central region where the pronounced electron jetting is located [*Daughton et al.*, 2006; *Karimabadi et al.*, 2007; *Shay et al.*, 2007]; the arms have a finite thickness perpendicular to, but inside the mathematical separatrices. Electron agyrotropy near the X-separator and parallel to the exhaust is usually seen in the PIC code as two stretched, quasi-parallel and slightly curved ribbons, with a third ribbon at times between these two which look like the two ribbons of agyrotropy seen in the Harris equilibrium illustrated below.

4. Agyrotropy Is Presently Detectable

[16] We use Figure 2 to illustrate that plasma detectors already flown in space are in principle sufficiently capable to determine agyrotropy of the size seen in the examples throughout this paper. We show the fractional difference in perpendicular eigenvalues of the pressure tensor as function of the size of agyrotropy. Agyrotropy of $A\emptyset_e = 0.1$ (0.65) corresponds, for example, to a 10(100)% difference in the

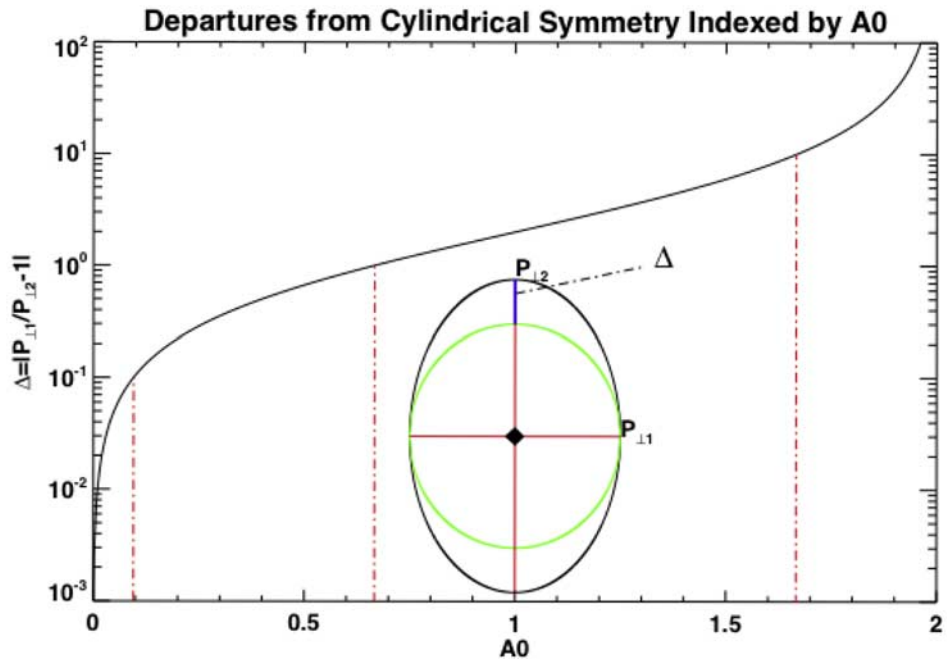

Figure 2. Relationship between agyrotropy and percentage separation of perpendicular eigenvalues of pressure tensor. These values are like the energy e-foldings of the distribution function. Agyrotropy of the size suggested in Figure 1 and elsewhere are well within present electrostatic analyzer detector capabilities. Temperature eigenvalues are strictly proportional to pressure eigenvalues.

"temperature" ($T_{\perp e} = P_{\perp e}/nk$) e-folding energy half-widths of f_e (**v**) that must be detected when analyzing f_e (**v**) along two orthogonal directions, both perpendicular to **B**.

[17] Typically the temperature eigenvalues are accurate to a few percent, so that such $A\emptyset_e$ is readily discernible with well calibrated electrostatic analyzers designed for space flight. In this light, nearly all the brightly colored signatures in Figure 1 are detectable with present instrumentation [cf. *Scudder et al.*, 2002, 2008]. However, the electron agyrotropy is only as precise as the model independent determination of the pressure tensor (evaluated in the electron's rest frame). The observed velocity distribution in space plasmas f_e (**v**), is actually acquired over an interval of time, and is usually a convolution over variations in $\hat{\mathbf{b}}$ and background variables during their acquisition – in contrast with the snapshot character of the same information from a PIC code. In addition, the quality of spaceflight estimates of f_e (**v**) hinge on the Poisson statistics of the measurements (see Appendix B), the time aliasing interval, the underlying variations of the plasma traversed, and the size of focusing, the size of the spacecraft potential, whether the spacecraft is an equipotential or not, and the detailed mounting of the sensor apertures relative to the spacecraft skin. Agyrotropy detection may not be easy, but the PIC simulations highlight their potential benefits.

[18] With a well calibrated electron plasma detector on a small, equipotential spacecraft the subsequent data analysis stream should have a near zero modal value of agyrotropy. Sporadic violations of gyrotropy as exceptions of the more common gyrotropy have been reported near a magnetic null at the earth's magnetopause [cf. *Scudder et al.*, 2002, section 6]. Recently, departures from gyrotropy have been reported in "guide geometry" layer near the cusp using Cluster data (D. E. Wendel et al., Magnetic structure and particle flow at a northward interplanetary magnetic reconnection site, submitted to *Journal of Geophysical Research,* 2007), but no baseline of routine gyrotropy recovery was presented, nor was a baseline of recovery of electron bulk velocity versus $\mathbf{E} \times \mathbf{B}$ determinations in unperturbed regimes documented. Certainly all such suggestions of detection of agyrotropy should be held to the highest experimental standards of scrutiny, particularly for their susceptibility to convolution effects and/or sensitivity to the precise time order of data acquisition. In particular, sensors that rely on slow spacecraft spin to acquire full sky coverage in velocity space will be especially disadvantaged in this quest to determine agyrotropy. Similarly, any technique for acquiring the distribution that cannot address the underlying reorientation of the magnetic field during the assembling of f(**v**) will also suffer from serious aliasing. These two brief sentences highlight the experimental challenge for observing agyrotropy. This paper is about the rewards for undertaking this challenge either with experiments up to the difficulties, or, possibly the design of instruments and measurement chains optimized for its detection, such as might be possible on the upcoming MMS mission. The local and "event" character of agyrotropy for reconnection studies are persuasive motivators to design spacecraft measurement sequences that allow in flight intracalibration of multisensor analyzers and post measurement assessments of possible time aliasing, to

yield the pressure tensor asymmetries beyond anisotropy [*Holdaway et al.*, 2008].

5. Agyrotropy Determinations From PIC Simulations

[19] Is the precision of $A\emptyset_e$ in Figure 1 adequate to guide an experimental search for features in the EDR? From an "experimental" perspective a snapshot of the PIC code solution is free from detector intracalibration issues, spacecraft potential effects, and totally uncompromised by time aliasing issues. If there are systematic difficulties with computing $A\emptyset_e$ these may be studied in a more controlled way in the PIC environment than with spacecraft data directly. In this section we document a procedure for determining agyrotropy, once the full electron pressure tensor is known. We then demonstrate recovery by our procedure of the analytically known agyrotropy for the initial Harris equilibrium with background. Common conceptual issues between PIC and spacecraft determinations of $A\emptyset_e$ have been identified and overcome by this approach. Succinctly, the apparent broken cylindrical symmetry $A\emptyset_e$*, determined directly from the pressure tensor can depend on the number N, of particles that approximate the underlying velocity probability distribution f_e (**v**). Fortunately there exists a first order approach to correct for this sensitivity to more nearly recover a better approximation of the Vlasov agyrotropy diagnostic we desire.

[20] In PIC and space applications the actual amplitude of the sensitivity depends on the method of integration used to determine the pressure tensor; however, the scaling of these effects in both domains goes like $N^{-1/2}$ where N is the number of computational particles per cell. The finite size of N guarantees there is a limit to the symmetry breaking than can be determined by f_e (**v**), approximated by N particles. With a finite number of particles approximating the velocity distribution function, even a truly gyrotropic "parent" f(**v**) would be approximated in PIC by a "bumpy" distribution with a computed agyrotropy $A\emptyset$*, that would have a finite N, "discreteness" contribution that would disappear in the large N limit. With PIC and space measurements pragmatic choices determine the achievable sizes of N. However, N in a given cell (spectrum) is also a function of time and will have different values as the dynamics of the CMR proceeds or the spacecraft moves through plasma regimes.

[21] Before tackling the spatial and time dependent nature of this difficulty we attack a simpler problem: "What is the computed agyrotropy $A\emptyset$* when N-particle distributions are drawn from Vlasov gyrotropic parent distribution"? In Appendix B we answer this question by establishing the inverse square root dependence of this artifact for $10 < N < 10^6$ and determine for our PIC code the proportionality constant, power law and their errors by a least squares procedure. We also establish there that repetitive draws of N particles at random from a gyrotropic distribution yielded log normal deviates from the best predictor at a given N. Knowing the statistics of this noise term we calculate at various levels of precision in Appendices C and D the expected functional relationship between apparent agyrotropy $A\emptyset^* = \mathbb{Z}(A\emptyset, N)$, assuming a general, nonzero underlying Vlasov value $A\emptyset$, and N. This relationship is generally invertible, so that knowledge of N and $A\emptyset$* can predict a significantly more accurate value of $A\emptyset = \mathbb{Z}^{-1}(A\emptyset^*, N)$. This inverse interpolation "compensation" procedure is different than subtracting a floor that is a function of N alone, since when $A\emptyset$ is large enough the discreteness effects are negligible, whereas the floor procedure would erroneously reduce peak agyrotropies in such a regime. As illustrated by the surface for $\mathbb{Z}$ in Appendix C, different parts of a spatially inhomogeneous solution will have varying degrees of correction applied by this procedure. Figure 1 above was constructed with this compensation technique and is our best representation of $A\emptyset_e$ for that PIC solution.

6. Recovery of Analytic Results for $A\emptyset$ of Harris Equilibrium With Background

[22] To demonstrate the quality of this procedure we consider the recovery by it of the analytically known agyrotropy of the Harris equilibrium with background. This approach does not endorse the Harris plus background model as appropriate for any geophysical regime. We only use it as a model to "test" parameter recovery of our agyrotropy determinations. The antiparallel Harris sheet model has a density profile $\boldsymbol{n}(\chi) = n_o \,\mathrm{sech}^2\chi$, a stationary background at the same species temperatures with density $n_b \equiv \varepsilon\, n_o$. Each species bulk speed U_j is its diamagnetic drift speed. Identifying species gyroradii ρ_j (defined at the asymptotic B far away from the current sheet) such a sheet has equilibrium, species dependent agyrotropy of the form

$$A\emptyset_j^{Harris} = \frac{2n_b n_o U_j^2}{w_j^2(n_o \mathrm{sech}\chi + n_b \cosh\chi)^2 + n_b n_o U_j^2} = \frac{2\varepsilon\rho_j^2}{L^2(\mathrm{sech}\chi + \varepsilon\cosh\chi)^2 + \varepsilon\rho_j^2}, \quad (2)$$

where $\chi = x/L$ is the dimensionless coordinate orthogonal to the sheet, L is the density's scale length and w_j is the jth species thermal speed. Agyrotropy results from the flow shear between the diamagnetic drift current layer and the static background; the last form of (2) illustrates that the agyrotropy at current sheet maximum is proportional to the fractional background density ε and the square of the species gyroradius. The left (right) column of Figure 3 illustrates the analytic trends of (2) with distance χ from the minimum in B for an ion (electron) gyro scale current sheets. The solid (dashed) trace is the ion (electron) agyrotropy profile in the chosen density scale current sheet. In either column we see (i) both ion and electron profiles have global maxima, two ribbons, at the same dimensionless distance on either side of the sheet given by the expression

$$|\chi^{\dagger}| = \ln\left(\frac{1+\sqrt{1-\varepsilon}}{\sqrt{\varepsilon}}\right) \quad (3)$$

determined by ε (chosen here to be 0.3); [The proton maximum in the electron sheet is only 1 part in a million

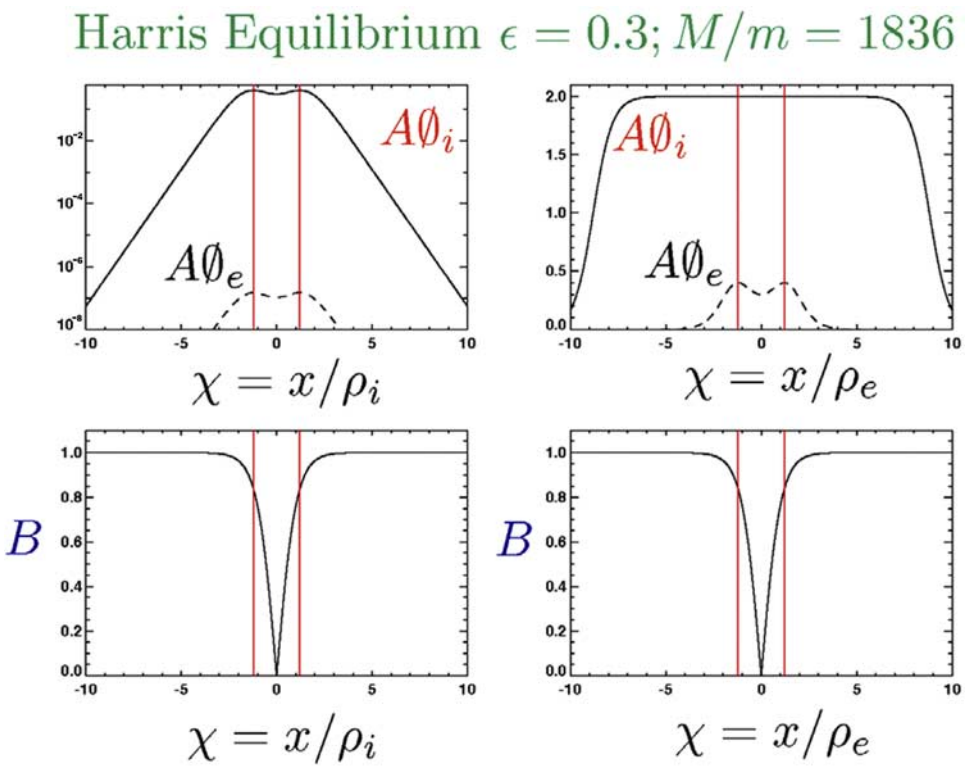

Figure 3. Harris Sheet with background ε = 0.3 for ion (electron) gyroradius scale current layer left (right), M/m = 1836. Upper rows are predicted agyrotropy from (2) of ions (electrons) with solid (dashed) curves. Ion A$\emptyset_i$ is invariably larger than A$\emptyset_e$. With the ceiling on agyrotropy of 2, the electron scale layer allows rather large electron and ion agyrotropies in the same layer, while ion scale current layers have a negligible electron agyrotropy at true mass ratio. Comparing with Figure 3, A$\emptyset_e$ is clearly expected to be detectable in Harris sheet with background if L approaches the electron gyroscale. Lower row illustrates the magnetic field strength. The spatial scale of left column is $\chi = x/\rho_i$ while the right hand side is much narrower in physical space $\chi = x/\rho_e$. Upper right panel illustrates that local symmetric minimaxes $|\chi^{\dagger}|$ of ion and electron agyrotropy (red vertical lines) in the same current sheet occur at the same spatial distance from current sheet center and is displaced from minimum B. This is also true in right hand panel, but the minimax is only 1 part in a million larger than value at current sheet maximum.

higher than the nearby parts of the ion profile.]; (ii) the agyrotropy at the current sheet crossing is enhanced but usually not the global maximum; (iii) the profiles of agyrotropy are rapidly attenuated, approaching gyrotropy with distance from the current sheet; (iv) the ion agyrotropy is always larger than the electrons at current sheets of either scale; and the expected values of $A\emptyset_e$, would be much (!) more detectable with present-day space plasma measurements at electron scale layers than ion ones (compare Figure 2).

[23] After the macro-particle distributions were formed using random number generators from a parent Vlasov Harris plus background equilibrium, the two eigenvalues perpendicular to **B** of the ion and electron pressure tensor were determined using the methods of Appendix A. The two columns of the top (bottom) row of Figure 4 contrast two spatial averaging approaches for recovering the initial Harris ion (electron) agyrotropy for an ion scale equilibrium, $m_i/m_e = 100$. Each panel in Figure 4 contains three estimates of the agyrotropy based on the PIC pressure tensor: (i) the expected theoretical variation (black) from (2); (ii) the best, approximately Vlasov, agyrotropy $A\emptyset_i$ determined from the initial distributions of the PIC code (red) using the method outlined in Appendix A, with discreteness effects remediated via Appendix D; and (iii) a blue trace that is the direct, or raw, agyrotropy $A\emptyset_j$* determined from the PIC pressure tensor by the methods of Appendix A, without any corrections for the effects of "discreteness." In symbols

$$A\emptyset_j = \left\langle \mathbb{Z}^{-1}\left(A\emptyset_j^*(\langle \mathbf{P}\rangle_{XY})\right)\right\rangle_{\text{Ignorable}} \tag{4}$$

where $\mathbb{Z}^{-1}$ stands for the reconstruction operation outlined in Appendix D that compensates for the effects of the finite number of simulation particles. The last spatial averaging performed is over the ignorable coordinate of the equilibrium in the simulation plane. Spatial averaging $\langle\ \rangle_{XY}$ was performed over a square of simulation cells centered on the desired cell, using an odd number of cells on a side.

[24] The results of using two different sized XY spatial averages of the pressure tensor elements are illustrated in the two columns of Figure 4: (i) a more vigorous spatial averaging over 7 × 7 squares in the left hand column is contrasted with (ii) no spatial averaging in the right hand column. The full scales on the electron (vs ion) panels are

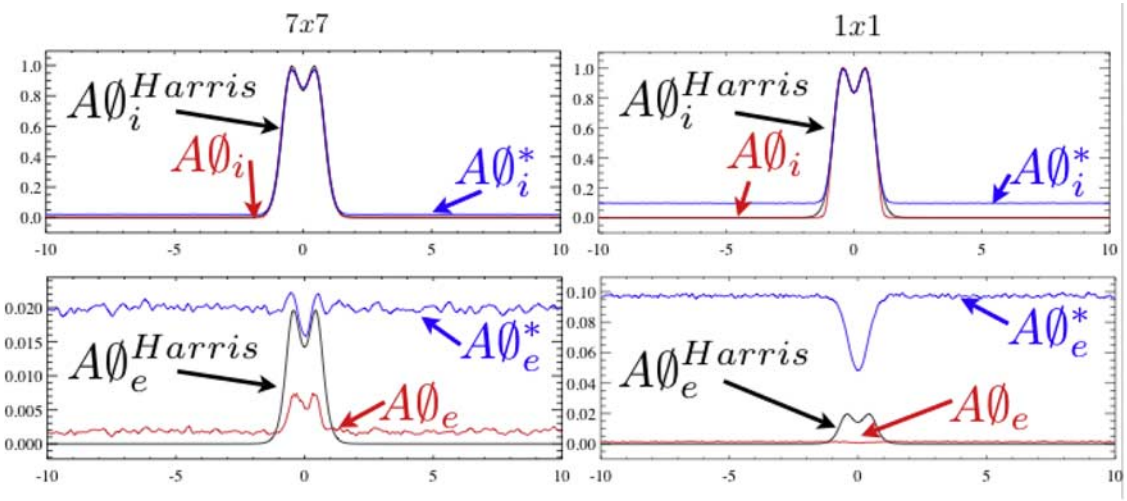

Figure 4. Demonstration of recovery (red) of theoretical agyrotropy (in black) of initial Harris sheet equilibrium. Antiparallel Harris equilibrium 100 × 100d_i, m_i/m_e = 100, sheet thickness $\rho_i/L = 2$ and $T_e = T_i$. Left column: agyrotropy determined by first averaging pressure tensor elements over spatial grid 7 × 7 centered on the desired mesh point. Right column: no spatial averaging of the pressure tensor elements. All figures contain 3 curves: (i) black is the Harris analytical profile; (ii) blue is the raw agyrotropy AØ* from techniques of Appendix A only; (iii) red is the best estimate of the Vlasov agyrotropy given the discreteness effects, using techniques of Appendices A and D. Top row demonstrates strong ion agyrotropy. Lower row demonstrates expected weaker initial electron agyrotropy (black) of the Harris equilibrium. Blue curves reflect all contribution including discreteness in AØ*.

chosen to illustrate (i) the much smaller initial, analytical electron variation of the agyrotropy (black curves) at a current sheet with ion scales, (ii) the clues concerning discreteness that the electron processing for agyrotropy provided, and (iii) the mitigation of discreteness effects enabled by the post processing discussed in Appendix D.

[25] Far away from the current sheet (at large |x|) the blue traces for ions and electrons in the same column of Figure 4 give essentially the same values for $A\emptyset_j$ (note scale differences); these residual values are determined by the number of particles per cell, which is virtually the same in these regions. However, these values are *incorrect*, as can be seen by comparing them with the much lower analytical predictions (black). Within species, but across columns, as averaging and N increase, the blue curves at large |x| are strongly reduced, demonstrating better recovery of gyrotropy and agreement with the black theoretical curve. As the lower row of electron panels exhibit, this averaging helps to correct for discreteness noise (a) by reducing it, even though (b) it is incomplete, (c) and does not retrieve with high fidelity the very weak analytically expected initial agyrotropy signal (black) in the electrons at early times starting with an ion scale Harris sheet and background. Nonetheless the discreteness correction does "remove" the erroneous impression of the raw agyrotropy (blue) that the electrons are more gyrotropic in the current sheet than outside!

[26] Strong ion agyrotropy is expected at this current sheet since the scale of the sheet is comparable to the ion thermal gyroradius (see equation (3) and left columns in Figure 3); the ion profiles (red in top row of Figure 4) compare favorably with the analytical solution (black) from equation (3). The recovery for ions of the twin peaked shape and amplitude is generally excellent, particularly at the highest values of agyrotropy in the right column (with no grid averaging) and almost as good with wider averaging (left column) and even better (than no averaging) at smaller absolute values of agyrotropy when vigorous averaging is undertaken (left column). While enhancing the statistics, the spatial averaging can, however, broaden the profile of agyrotropy. In the left hand column, the spatial width represented by the spatial averaging is comparable to the scale of the curvature scale of the peak in the agyrotropy profiles, thus causing a slight, but perceptible, smoothing of the inferred profile at and near its peaks (left hand column top row). By contrast, the no grid averaging in the right column recovers the strongest agyrotropy nearly perfectly throughout the maximum region. However, slight disagreements remain in the no averaging column as the black and red profiles plummet toward gyrotropic levels. This region is the part of the agyrotropy recovery curve near the "noise" floor agyrotropy identified in Figure D1 (Appendix D), when adjusted for the effective number N in that locale. The better statistics of averaging over 49 cells in the presence of relatively broad scale of the large |x| variation allows the vigorous averaging (upper left) to recover the details of the ion transition to the background gyrotropy, including very low values outside the sheet.

[27] For perspective the evolving amplitudes of electron agyrotropy in reconnecting current sheets, as shown in Figure 1, are comparable to the much larger, initial $A\emptyset_i$ values that our procedures recover well in the top row of Figure 4. This can be understood from the thinning of the initial ion scale sheet as reconnection gets underway, rapidly becoming an electron scale current sheet. We conclude that our technique can measure electron or ion agyrotropy provided the signal is strong enough (which we make quantitative between Figures 4, B1, and D2 below). We have examined other current sheet equilibria (not shown)

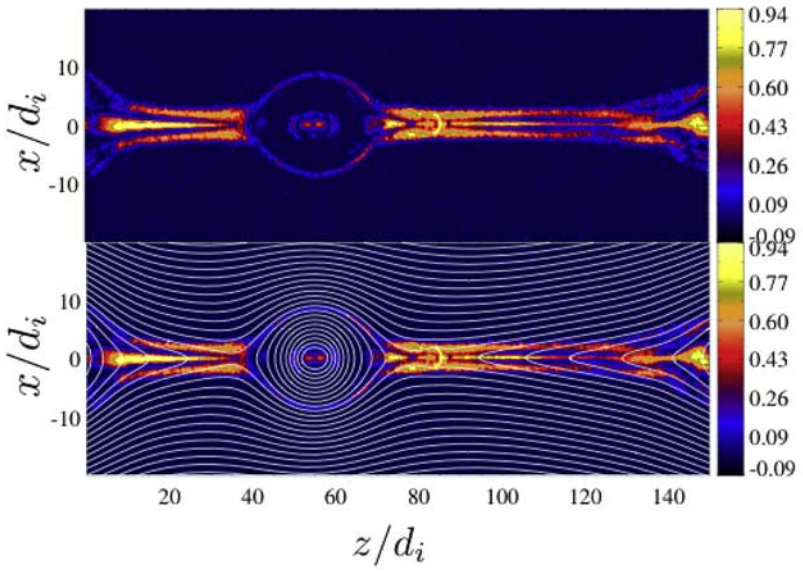

Figure 5. Pair plasma in very long system discussed by *Daughton and Karimabadi* [2007], contrasting "O" diagnosis and attendant double pear shaped pattern of agyrotropy with the different pattern about the X lines seen near z/d $_i$ = 90. Whatever causes the intensified layers is not controlled by whistler physics which is precluded in the pair plasma considered here.

where the peak ion agyrotropy was smaller (0.45) and obtained similar recovery as illustrated in Figure 4. In a pair plasma, where the electron and ion agyrotropy should be identical we have recovered the analytical spatial profiles for both species with equal precision.

7. Associating Agyrotropy and Toplogical Boundaries

[28] We now illustrate a variety of PIC simulations of CMR at Harris current sheets using the lens of $A\emptyset_e$. All simulations use the open boundary condition code fully described by *Daughton et al.* [2006]. Figure 5 establishes the spatial pattern of $A\emptyset_e$ near "O" points in a pair plasma layer, confirming the suggestion of *Bessho and Bhattacharjee* [2005] that the gyroviscous effects of electrons and ions cooperate to balance the electric field in this layer. This example illustrates that the intensification of agyrotropy occurs near X and O point with different patterns. Near the "O" point there usually are two opposing pear shaped enhancements of agyrotropy, inscribed by elliptical or nearly complete ellipses concentric with the O line. In contrast with the "X" separator in Figure 1 there is no suggestion of an enhancement of agyrotropy forming a crossing ribbon pattern like the separatrices seen in the center of Figure 1. From the lower panel of Figure 5 the outermost elliptical ring about the O line is actually the continuation of the nearby "X" point separatrices as they nest the adjacent "O."

[29] The size and extent of the demagnetized current layer undergoing tearing is highlighted by $A\emptyset_e$ in Figure 6 for the

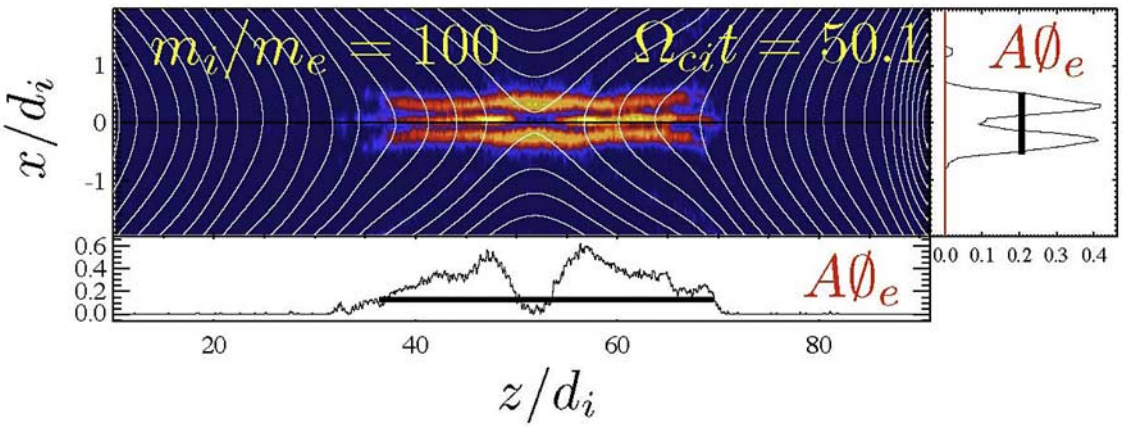

Figure 6. Antiparallel Harris equilibrium, open boundary conditions, $m_i/m_e = 100$. Note that the vertical axis of the figure is grossly magnified relative to the horizontal axis with the purpose of illustrating the demagnetized Electron Diffusion Region structure along the in and outflow. This differential magnification greatly reduces the apparent length to width aspect ratio.

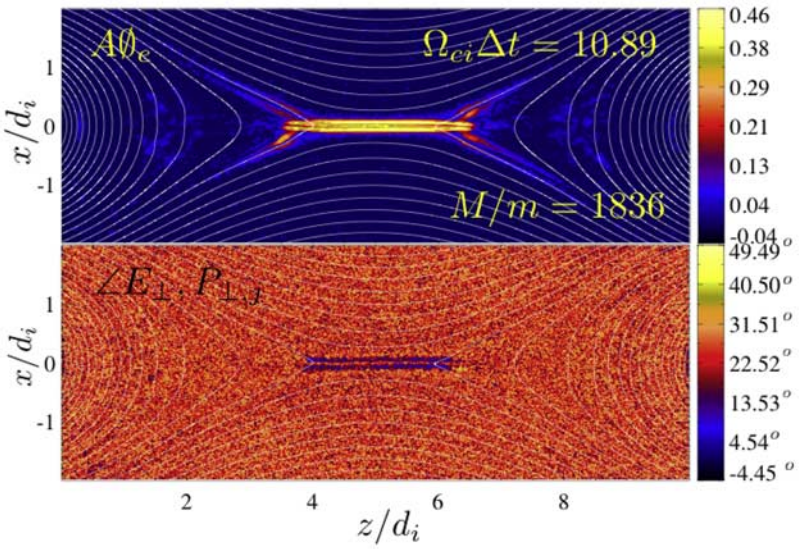

Figure 7. (top) Agyrotropy obtained from open boundary simulation with hydrogen mass ratio (m_i/m_e = 1836). (bottom) Lower panel illustrates the smallness of the angle between perpendicular E and the closest perpendicular eigenvector of the electron pressure tensor in the region of strong agyrotropy illustrated in the upper panel. Note that if the eigenvector's phase becomes random (as in gyrotropy) or the perpendicular electric field becomes weak and not well ordered that 22.5° is the "no signal" result. This accounts for the common occurrence of red-orange colors in region where $A\emptyset_e$ is small and becoming more gyrotropic.

antiparallel, m_i/m_e = 100 perturbed Harris sheet discussed by *Daughton et al.* [2006] and *Karimabadi et al.* [2007]. The electrons in the inflow region are clearly suggested to be magnetized by our remediated diagnostic. Furthermore, for the purposes of this figure there is no analog to averaging over ignorable coordinate in (5) since the evolving layer has no ignorable coordinate in the solution plane. In spite of that loss of statistics the remediation technique does "correctly" indicate that the electrons in the inflow are strongly magnetized. Without ambiguity this demagnetized layer possesses an ion scale length along its exhaust of ($15d_i = 150d_e$) from the separator, while only exhibiting an electron scale width ($0.4d_i = 4d_e$) along the corresponding part of the inflow (vertical). These measurements yield an elongated aspect ratio (length/width) of the demagnetized rectangular portion of the EDR of 37. The demagnetized layer is somewhat larger than the out of plane current sheet which has length to width ratio of 23 which is still large compared to the early assumptions that-the EDR had scales ratios of approximately 5, a "few" electron skin depths or electron turning orbits on a side. The electron pressure tensor is non-gyrotropic in a spatially structured way that influences the mechanical force balance [*Karimabadi et al.*, 2007] over the multiple ion scale electron jet outflow length of over $\pm 15d_i = \pm 150d_e$, a point recently conceded by *Shay et al.* [2007]. In the present context we wish to emphasize the crucial diagnostic role of agyrotropy, especially as it becomes small, since it has been used to determine the physical extent of the critical non-ideal electron diffusion region (EDR) of the layer. Shown in the right inset, the antiparallel reconnection EDR has a bifurcated agyrotropy profile along the inflow direction as has been seen in Figures 1 and 4 with the guide field examples and is also present in the Harris equilibrium of Figure 3. The two parallel ribbons of enhanced agyrotropy persist even after strong reconnection is underway, with a third intervening ribbon substructure straddling the exhaust lane in both directions.

[30] The possible utility of agyrotropy for finding a reconnection current sheet with the hydrogen mass ratio of m_i/m_e = 1836 is illustrated in Figure 7; the two panels contain different diagnostics relevant to the formation of agyrotropic layers in CMR. Having evolved from an ion scale antiparallel Harris equilibrium with background, the top panel shows strong, bifurcated parallel ridges of electron agyrotropy (with magnetic flux surfaces superposed) with values peaking at easily measurable amplitudes of 0.5 that would be accompanied by perpendicular electron temperature eigenvalues that differed by 70% (see Figure 2). While the length of the rectangular jet region of the EDR is smaller at this larger mass ratio, its length to width ratio is still large: 20. With resource limitations this simulation was quite small ($10 \times 10)d_i$ and the simulation time was short; accordingly it may not be the definitive length to width ratio that might be achieved in larger/longer simulation. However, for our present purposes this simulation illustrates that agyrotropy is strong even in systems with the mass ratio relevant for NASA's upcoming MMS mission. Extensions of enhanced agyrotropy also are seen to occur along the separatrices (light purple) as in the previous examples at lower mass ratios. Even the weak enhanced agyrotropy along the separatrices is in strong contrast with the highly magnetized (dark blue) (low agyrotropy) near gyrotropy recovered by this analysis (via Appendix D) in the inflow region.

[31] The lower panel of Figure 7 hints at the driving force behind the agyrotropy layers seen in the upper panel. Illustrated there is the spatial variation of the angle between

the perpendicular electric field and the closest perpendicular principle axis of $\vec{\vec{P}}_e$. At the inflow sides of the diffusion regions along the strong quasi-parallel ribbons of enhanced agyrotropy, this angle becomes systematically smaller, with perpendicular eigenvectors nearly aligned with the direction of the perpendicular electric field. This angle remains small throughout the enhanced rectangular jet region of the EDR that extends in the horizontal directions and supports the exhaust. Patterns of darker red can also be seen for this angle out along the separatrices. Elsewhere, when the electric field is either small or oriented at random with respect to the perpendicular axes of the pressure tensor this angle reverts to 22.5°, since the closest perpendicular eigenvector is never farther than 45° away for any $\hat{\mathbf{E}}_\perp$. (When the plasma is nearly gyrotropic the orthogonal eigenvectors associated with the nearly degenerate eigenvalues can always be found; the degeneracy of the eigenvalues assures that the eigenvectors identified will generally be phased at random in the plane perpendicular to **B**; this degeneracy for the gyrotropic plasma leads to the relatively widespread occurrence of the orange ''default'' regions with nearly 22.5°.)

[32] The lower panel in Figure 7 is consistent with the premise that direct non-adiabatic interactions of the electrons and the electric fields in these layers can preferentially deform and locally sustain the velocity space agyrotropy there and deform $f_e(\mathbf{v})$ with a pattern that is coherent on the timescale of the forcing perpendicular electric fields. These patterns evolve slowly and are not changing on the electron gyroperiod as has been verified by determining their patterns using individual output frames of the solution without time averaging. The self-consistent PIC orbit simulations of this paper substantiate the test particle Vlasov mappings and suggestions of *Scudder and Mozer* [2005] that short scale electric field layers detected with Polar might be able to demagnetize the electrons in this way.

[33] It should be clear however, that neither the electric field, agyrotropy nor velocity shear are by themselves properly viewed as the cause or effect in these highly structured and nonlinear flows, since they are part of a slowly evolving quasi-equilibria. When describing this self consistent situation, however, it is easier to see the electric field as a force felt on individual electrons than that supplied, for example, from velocity shear. The demonstration by *Mahajan and Hazeltine* [2000] that there are Vlasov equilibria that are generalizations of the Harris equilibria that require equilibrium $A\emptyset_e$ and electric fields in the presence of velocity shear is suggestive of the possibility, as seen in the PIC code, that there are slowly evolving nearby Vlasov-like solutions such as these.

8. Summary and Discussion

[34] We have presented a variety of current layers where reconnection is in progress as described in the most model free way that 2-D kinetic simulations allow, including open boundary conditions; in all of these layers there are pronounced patterns of enhanced electron agyrotropy that illuminate topological boundaries of the magnetic field that are known from the vector potential. We have documented the high precision of our ability to determine $A\emptyset_e$ from PIC simulations and have established well defined procedures to accomplish such determinations. We have also indicated the patterns of $A\emptyset_e$ reveal a complicated non-convex region of non-idealness that emanates from the separator and that these patterns are distinctly different for X vs O points.

[35] Valid determinations of sizable $A\emptyset_e$ indicate a severe disruption of the thermal electron gyromechanics. To our knowledge there is no known mechanism for producing agyrotropy short of recent time demagnetization of the thermal electron gas. Such a diagnostic is an electron specific, kinetic prerequisite for electrons in the EDR of CMR that should be contrasted with the indirect tests of magneto-fluid accelerations of the Walen type that find quasi-Alfvenic rotational shear layers (resolved RDs) that may or may not be the external flows of CMR.

[36] Agyrotropy is a scalar that can be determined from measurements in one spatial locale, and does not require the comparison of measurements in different locales, nor the determination of a special direction to detect its size (as in the ''out of plane component of some vector''). $A\emptyset_e$ also provides the local observer with tags of non-idealness along the time line of measurements, without (i) making a planar model, or (ii) making the assumptions of Faraday Residue/Walen tests, (iii) presaging the unknown third and assumed ignorable direction to implement the $\mathbf{E} + \mathbf{U}_e \times \mathbf{B}|_3$, or (iv) assuming strong **E** and maximum variance of **E** establishes the geometry of the layer.

[37] Electron agyrotropy is ideal as a local marker for electron scale layers warranting further study as part of the reconnection layers in both 3-D PIC codes and spacecraft data. Ancillary magneto fluid acceleration correlations in the same locale as $A\emptyset_e$ would improve the false detections of collisionless reconnection layers based on electron agyrotropy alone.

[38] The valid detection of electron agyrotropy on one spacecraft first requires the routine statistical recovery by the same instrument of small $A\emptyset_e$. Only in this context will larger values of $A\emptyset_e$ be noteworthy. Once such calibration has been demonstrated to be routine, the collected electrons' immediate prehistory becomes the ''detector'' of any and all recent sub-electron gyro scale or super-gyro frequency fluctuations encountered enroute to detection. It also can reflect convolved errors of slow time acquisition across spatial structures that may or may not be demagnetizing. At this juncture the protections against aliasing need to be studied on those events. If the prehistory is gyrotropic, the previously calibrated detector is self nulling, returning a very small agyrotropy.

[39] This paper has demonstrated the usefulness of careful determinations of $A\emptyset_e$ for identifying current layers comparable to the electron gyro scale which are thought to be essential to CMR. We have also discussed that defensible detections will require ingenuity and suitable safeguards in telemetry acquisition to protect the possible aliasing of the measurements. We have outlined several classes of data collection that are more susceptible to this type of problem than others. We have referenced our own early attempts to address these issues with the Polar Hydra detector that we know best. Unlike other recipes for finding the non-idealized regions of the EDR, it is directly associated with the demagnetization of the electron fluid in the plasma, which would disrupt the electron fluid's facile advection and consistent labeling of magnetic field lines. Furthermore, this

technique has more intrinsic sensitivity to non-idealness that attempts to finite difference the electron pressure tensors across multiple spacecraft, since such techniques are limited by the finite difference error controlled by typically ion scale of spacecraft separation, and the need to control, document and remove the experimental vagaries of potential, focusing, measurement and cross instrument calibration for at least four different locations [*Henderson et al.*, 2006]. Even if all vehicles could be calibrated at the same level of precision, the errors of finite differencing on an ion inertial separation scales, looking for structures with electron spatial scales, makes such an experimental determination uninterpretable.

Appendix A: Inferences of Agyrotropy From the Full Pressure Tensor

[40] Any pressure tensor can always be diagonalized. However, when the plasma is not gyrotropic there is no guarantee that any of the eigenvectors will be aligned with or perpendicular to the magnetic field direction, $\hat{\mathbf{b}}$. Since we are explicitly interested in the departure from cylindrical symmetry about the local magnetic field, we wish to characterize the velocity distribution function's weighted average of dispersions of velocity vectors perpendicular to the magnetic field in the electron's zero momentum (center of mass) frame. We are thus interested in the symmetric tensor $\overleftrightarrow{\aleph}$ defined by

$$\begin{aligned}\aleph_{ij} &= m\int\int\int d^3\mathbf{v} f(\mathbf{v})\left(\mathbf{w}\times\hat{\mathbf{b}}\right)_i\left(\mathbf{w}\times\hat{\mathbf{b}}\right)_j \\ &\equiv \sum_{q,r,l,m}\varepsilon_{iql}\varepsilon_{jrm}\hat{b}_q\hat{b}_r P_{lm}\end{aligned} \tag{A1}$$

which is related to the full pressure tensor usually saved in a PIC code by the trailing identity. We have used $\mathbf{w}$ as the velocity of the particle in the zero momentum frame and ε_{ijk}, the fully antisymmetric Levi-Civita tensor. The six unique elements of $\aleph_{ij}$ are related by (A1) to those of the usual pressure tensor by the relations:

$$\begin{aligned}\aleph_{xx} &= b_y b_y P_{zz} - b_y b_z P_{yz} - b_z b_y P_{zy} + b_z b_z P_{yy} \\ \aleph_{xy} &= -b_y b_x P_{zz} + b_y b_z P_{zx} + b_z b_x P_{yz} - b_z b_z P_{yx} \\ \aleph_{xz} &= b_y b_x P_{zy} - b_y b_y P_{zx} - b_z b_x P_{yy} + b_z b_y P_{yx} \\ \aleph_{yy} &= b_x b_x P_{zz} - b_x b_z P_{zx} - b_z b_x P_{xz} + b_z b_z P_{xx} \\ \aleph_{yz} &= -b_x b_x P_{zy} + b_x b_y P_{zx} + b_z b_x P_{xy} - b_z b_y P_{xx} \\ \aleph_{zz} &= b_x b_x P_{yy} - b_x b_y P_{yx} - b_y b_x P_{xy} + b_y b_y P_{xx}\end{aligned} \tag{A2}$$

[41] By construction one of the eigenvectors of $\overleftrightarrow{\aleph}$ is the magnetic field direction with eigenvalue 0. Accordingly the characteristic polynomial for the eigenvalues of $\overleftrightarrow{\aleph}$ must take the form

$$\lambda\left(\lambda^2 - \alpha\lambda + \beta\right) = 0. \tag{A3a}$$

where

$$\begin{aligned}\alpha &= P_{\perp 1} + P_{\perp 2} \\ \beta &= P_{\perp 1}P_{\perp 2}\end{aligned} \tag{A3b}$$

However, the expressions for $\{\alpha, \beta\}$ are implied by the eigenvalue problem for $\overleftrightarrow{\aleph}$ and are given by:

$$\begin{aligned}\alpha &= \left(\aleph_{xx} + \aleph_{yy} + \aleph_{zz}\right) \\ \beta &= -\left(\aleph_{xy}^2 + \aleph_{xz}^2 + \aleph_{yz}^2 - \aleph_{xx}\aleph_{yy} - \aleph_{xx}\aleph_{zz} - \aleph_{yy}\aleph_{zz}\right)\end{aligned} \tag{A3c}$$

and can be used to determine the remaining two non-trivial eigenvalues that correspond to eigenvectors, $\hat{\xi}_k$ that are perpendicular to the magnetic field. These are:

$$\lambda_{k_\pm} = \frac{\alpha \pm \sqrt{\alpha^2 - 4\beta}}{2} \geq 0, \tag{A4}$$

where the discriminant is given by the nonnegative expression: $\alpha^2 - 4\beta = (P_{\perp 1} - P_{\perp 2})^2$. When P is gyrotropic the discriminant vanishes. The two eigenvalues of (A3) establish the "equivalent" dispersion ellipse of P in the plane transverse to B, and should be identified with the two extremal temperatures transverse to B. Accordingly the agyrotropy at each spatial mesh location (i, j) of the simulation can be defined in terms of these eigenvalues by

$$A\emptyset_{ij} = 2\frac{\left|\lambda_{+,ij} - \lambda_{-,ij}\right|}{\lambda_{+,ij} + \lambda_{-,ij}} = \frac{2\sqrt{\alpha_{ij}^2 - 4\beta_{ij}}}{\alpha_{ij}} \geq 0 \tag{A5}$$

without recourse to eigenvalue or polynomial zeroing subroutines. This algebra permits the parallel computation across the simulation array of the dispersions transverse to B, making agyrotropy a routine diagnostic across the PIC simulation without generalized eigenvalue overhead. With simulations as large as 2560 × 2560, there are in excess of 6 million eigenvalue problems per time step, so the above efficiencies are enabling for this as a routine diagnostic. As PIC codes move into 3-D, the need for speed in this diagnostic and its role in finding diffusion regions makes speed all the more imperative.

Appendix B: Scaling of $A\emptyset^*$ With N When Plasma Is Gyrotropic

[42] For this scaling study 3000 gyrotropic phase space realizations were formed to understand the variation of directly computed agyrotropy $A\emptyset_j^*(N)$ (using the approach of Appendix A) as a function of the number N of simulation particles used to form the underlying pressure tensor in the PIC cell. If gyrotropic analytic Vlasov equilibria were analyzed, their computed agyrotropy would vanish by strict symmetry; thus any residual computational agyrotropy for these macroparticle approximations is a type of noise commingled with any physical agyrotropy that may be present. To quantify the expected error versus N of the same anisotropic, but gyrotropic, convecting velocity distribution, thirty independent trials were performed with each of 100 logarithmically spaced numbers, N, of macro-particles/cell. The underlying physical parameters of the Vlasov distribution were held constant across all realizations. For each trial $A\emptyset_j^*(N)$ was determined by the method of Appendix A. In this way the j'th realization of the "discreteness" floor for agyrotropy, $A\emptyset_j^*(N_o, j)$ when drawing N_o particles was determined, together with its

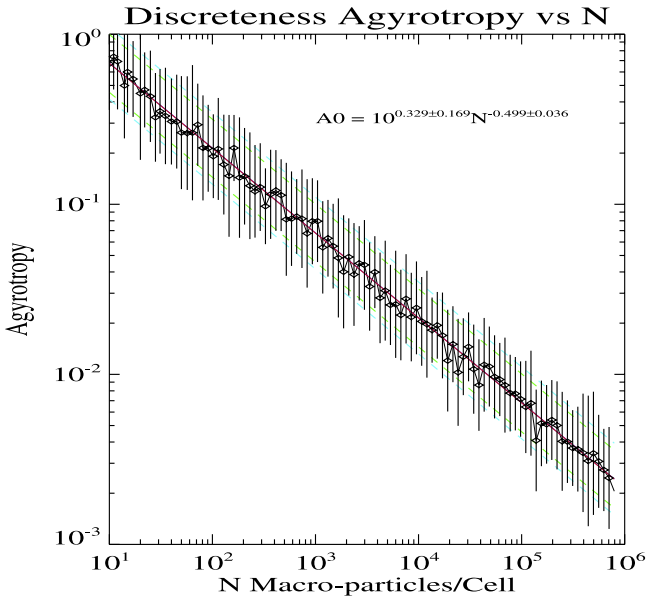

Figure B1. Summary of determination of ''Discreteness'' Agyrotropy, demonstrating inverse square root dependence on N. At each N, 30 trials were performed with mean at the diamond and error flag reflecting the variance.

average $\langle \mathrm{Log}\, A\emptyset^*_f(N_o, j)\rangle_j$ and variance over the 30 different trials when drawing the same number of particles. Figure B1 demonstrates the recovery of the expected inverse square root dependence of the ''discreteness'' agyrotropy, together with a least squares regression to power law variation that fits the data very well. This variation is summarized by the relation (with errors at 3σ):

$$A\emptyset_{FLOOR}(N) = 10^{0.329\pm0.169} N^{-.499\pm0.036} \tag{B1}$$

[43] We have also shown that this scaling is independent of temperature, anisotropy, bulk speed and mach number and, that the 3000 deviates from the best fit line in Figure 3 have a lognormal distribution. For a simulation with 2560 $\times$ 2560 cells and 1.5 billion particles, N in the average cell in a uniform density simulation contains upwards of 228 particles. Initially the density is 4 times higher in the narrow current layer, corresponding to somewhat less than 4 times the typical occupation number, making a peak value for N of approximately 900/cell. In practice, as many as three successive output time frames for a given cell are time averaged together to enhance the particle statistics without degrading spatial resolution. In this way the peak effective number of particles in some cells for agyrotropy estimates can easily be upwards of 2700, lowering the discreteness floor to 0.02 in the high density regions at the expense of time resolution. Including box spatial averaging with W cells on a side reduces this floor further to approximately 0.02/W. At other places in the simulation, however, discreteness is more important because the density is nonuniform and can become lower than average.

[44] If the discreteness contribution can be modeled and understood as presented in Appendices C and D, the recovery of even smaller agyrotropies is feasible, although with higher reconstruction errors than those above 0.02/W. Since the nonzero size of agyrotropy is used to determine the spatial extent of the EDR [*Karimabadi et al.*, 2007] it is important to pursue reconstruction of the profile as the gyrotropic regimes is approached. As can be seen in Figure 1, the inflow regime to the separatrices (along the vertical) is characterized by very low values of agyrotropy, consistent with our theoretical view that the electrons advect the field in this region and hence should be nearly gyrotropic with $A\emptyset_e \downarrow 0$. Because the number of particles in a given cell is dynamic across the simulation, a reconstruction technique is required that can handle the case of a general occupation number N; only in this way can the structure in space be truly suggested to reflect that of the Vlasov fluid. The reconstruction (discussed in Appendix D) can make a significant correction for this discreteness floor when N is smaller than when it is larger, as illustrated by the overlay of the red and black ion curves in Figure 3 (top row) and Figure D1. During reconnection in a Harris sheet a strong density depression develops at the separator where we seek to understand the microphysics. Lower occupation numbers in the low density inflow to the current sheet will also require significant remediation as has been achieved in Figure 3 and Figure 1. Determinations of the spatial variation of agyrotropy in these locales is also affected and improved by the reconstruction corrections of Appendix D.

[45] After this discreteness correction the Vlasov inferred agyrotropy is reduced at large distances from the current sheet to quite small values and we do recover the extremely weak agyrotropy of the Harris equilibrium suggested by the red curve (in Figure 3) at large distances from the current sheet. The initial electron agyrotropy in this $m_i/m_e = 100$ equilibrium is down by a factor of 50 from that of the ions, well beneath the floor of detectability, even after reconstruction has been attempted. However, as the layer reconnects, velocity shears, electric fields and electron agyrotropy build up to comparable amplitudes as those present in the ions in the equilibrium, making the PIC diagnosis of these layers possible at all but the earliest simulation times (see Figure 1). Our reconstruction studies and others not presented here can be interpreted to say that PIC agyrotropies in either species of the size reported in Figures 1 and 3 are clearly detectable and the reconstructed spatial variations (black curves in Figure 3) are indeed representative of the smooth underlying Vlasov behavior.

Appendix C: Simple Model for Expected Agyrotropy, $A\emptyset^*$ in Terms of the Underlying Vlasov Agyrotropy

[46] Assume for simplicity that the ''true'' underlying Vlasov agyrotropy is denoted by $A\emptyset$ while in the presence of Gaussian noise the computed agyrotropy would take on the form:

$$A\emptyset^* = \frac{\int_{-A\emptyset}^{\infty} (A\emptyset + \delta)\exp\left(-\frac{\delta^2}{\sigma^2}\right)d\delta}{\int_{-A\emptyset}^{\infty} \exp\left(-\frac{\delta^2}{\sigma^2}\right)d\delta} \tag{C1}$$

where the average taken presumes $A\emptyset + \delta \geq 0$. In this model the apparent agyrotropy $A\emptyset^*$ is equal to

$$A\emptyset^* = A\emptyset + \frac{\sigma}{\sqrt{\pi}} \frac{\exp\left(-\frac{A\emptyset^2}{\sigma^2}\right)}{1 + Erf\left(\frac{A\emptyset}{\sigma}\right)} \tag{C2}$$

Interpreting this result for the gyrotropic circumstance where $A\emptyset = 0$, yields the identification that

$$A\emptyset^*(A\emptyset = 0) = \frac{\sigma}{\sqrt{\pi}}, \tag{C3}$$

Since Figure B1 provides the left hand side of (5), we obtain

$$\sigma(N) = 2.5\sqrt{\pi} N^{-1/2} \tag{C4}$$

Rescaling (C2) we obtain for the *ij* simulation cell the convolving relationship:

$$\frac{A\emptyset^*_{ij}}{\sigma(N_{ij})} = \frac{A\emptyset_{ij}}{\sigma(N_{ij})} + \frac{1}{\sqrt{\pi}} \frac{\exp\left(-\frac{A\emptyset^2_{ij}}{\sigma(N_{ij})^2}\right)}{1 + Erf\frac{A\emptyset_{ij}}{\sigma(N_{ij})}} \tag{C5}$$

[47] Assigning dummy variables (C5) takes on the obvious functional form: $Y_{ij} = \mathbb{Z}(X_{ij})$, that is immediately amenable to one dimensional inverse interpolation, since (C5) is a one to one mapping. Thus

$$A\emptyset_{ij} = \sigma(N_{ij}) \mathbb{Z}^{-1}\left(\frac{A\emptyset^*_{ij}}{\sigma(N_{ij})}\right) \tag{C6}$$

and the reconstruction is complete.

Appendix D: Full Up Model: Expected Agyrotropy, $A\emptyset^*$ in Terms of the Underlying Vlasov Agyrotropy

[48] Below we retain the distinction in the text between the agyrotropy $A\emptyset^*$ available by direct manipulation of the computed pressure tensor (Appendix A) and the likely agyrotropy, $A\emptyset$ of the Vlasov fluid being simulated or sampled.

[49] Considering each eigenvalue determination to be a member of a log normal distribution, then

$$g_j = \ln \frac{P_{\perp j}}{P_{\perp j,o}}$$

is normally distributed in g, with most probable value $P_{\perp j,0}$. The expected average of such "noisy" determinations is given by the expression

$$A\emptyset^* = \frac{2}{\pi\sigma_1\sigma_2} \int_{-\infty}^{\infty} dg_1 \int_{-\infty}^{\infty} dg_2 \frac{|\exp(g_1 - g_2 + \Lambda) - 1|}{\exp(g_1 - g_2 + \Lambda) + 1} \cdot \exp\left(-\frac{g_1^2}{\sigma_1^2} - \frac{g_2^2}{\sigma_2^2}\right);$$

$$\Lambda \equiv \ln \frac{P_{10}}{P_{20}}$$

where the $\perp$ subscript has been suppressed. Assuming that the σ's are identical so that agyrotropy can be lognormal as well, and after change of variables $\chi = g_1 - g_2$; $\eta = g_2$ (Jacobian is unity), this double integral can be reorganized to a single integral of the form

$$A\emptyset^*(\Lambda(A\emptyset), \sigma) = \frac{2}{\sqrt{\pi}} \int_{-\infty}^{\infty} d\Gamma \exp(-\Gamma^2) \left|\tanh\left(\frac{\sigma\Gamma}{2^{1/2}} + \frac{\Lambda}{2}\right)\right| \tag{D1}$$

This numerically tabulated function represents a summary of the forward problem between states of definite Vlasov agyrotropy emulated by N macro particles and the apparent agyrotropy available via the moments and Appendix A. This relation is depicted in Figure D1:

[50] Since $\Lambda(A\emptyset) = \ln \frac{P_1}{P_2} = \ln \frac{2+A\emptyset}{2-A\emptyset}$, Vlasov gyrotropy implies $\Lambda = 0$; the expected averaged floor for $A\emptyset^*$ is only a function of the local number of particles in the cell as demonstrated in (D4) below:

$$A\emptyset^*_{Floor} \equiv A\emptyset^*(0, \sigma(N)) = 4\pi^{-1/2} \int_0^{\infty} d\Gamma \exp(-\Gamma^2) \tanh\left(\frac{\sigma\Gamma}{2^{1/2}}\right) \tag{D2}$$

This relation is illustrated by the red bounding curve in Figure D1. Additionally, if σ is appropriately small (D2) may be approximated as:

$$A\emptyset^*(\Lambda = 0, \sigma) \simeq 4\pi^{-1/2} \int_0^{\infty} d\Gamma \exp(-\Gamma^2) \frac{\sigma\Gamma}{2^{1/2}} = \frac{2\sigma}{\sqrt{2\pi}} \int_0^{\infty} d\Gamma \exp(-\Gamma^2) 2\Gamma = \sqrt{\frac{2}{\pi}}\sigma, \tag{D2'}$$

which when compared with the results of Appendix C illustrates that the individual pressure sigmas (of the log normal distributions so they are dimensionless!) is each half of the sigma of the agyrotropy.

[51] From PIC trials (Figure B1) it has been demonstrated that the directly computed agyrotropy for a random draw of N particles from a parent gyrotropic distributions satisfies the relation:

$$A\emptyset^{*\{-,0,+\}}_{PIC}(A\emptyset_{Vlasov} = 0) = 2.5 \times 10^{\{-.284,0,.284\}} N^{-1/2}. \tag{D3}$$

When (D2') is valid we recover the expected relationship that the sigma in the perpendicular pressures scales inversely with square root of the number of particles involved in emulating the distribution function $\sigma^{\{-,\ 0,\ +\}} \simeq 2.5\ \sqrt{\frac{\pi}{2}} \times 10^{\{-.284,0,.284\}}\ N^{-1/2}$.

[52] Reconciling (D3) and (D2) determines three implicit relationships for $\sigma(N)$ by the conditions:

$$2.5 \times 10^{\{-.284,0,.284\}} N^{-1/2} = 4\pi^{-1/2} \int_0^{\infty} d\Gamma \exp(-\Gamma^2) \tanh\left(\frac{\sigma_{-,0,+}(N)\Gamma}{2^{1/2}}\right) \tag{D4}$$

In every PIC cell or plasma sensor observation, the number N is known. From (D4) three values of $\sigma_{-\ ,o,\ +}$ may be determined from N by alternately using the mean and the two three sigma extremes of the amplitude of the fit synthesis embodied in (D3). In this way equation (D1) may

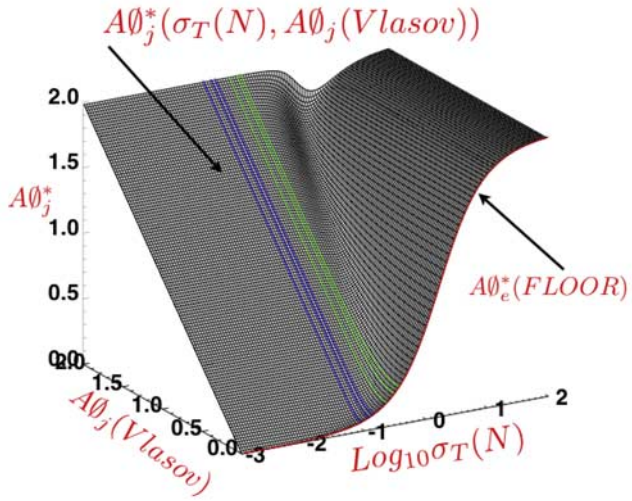

Figure D1. Map of the function relating Vlasov agyrotropy, the discreteness of the emulation of the Vlasov fluid and the apparent agyrotropy.

be recast at each N as three implicit equations for three relevant estimates of the Vlasov agyrotropy, $A\emptyset_{-,0,+}$:

$$A\emptyset^*_{PIC}(N) = \frac{2}{\sqrt{\pi}}\int_{-\infty}^{\infty} d\Gamma \exp\left(-\Gamma^2\right) \cdot \left|\tanh\left(\frac{\sigma_{-,0,+}(N)\Gamma}{2^{1/2}} + \frac{\Lambda\left(A\emptyset_{-,0,+}\right)}{2}\right)\right| \equiv \mathbb{Z}\left(A\emptyset_{-,0,+}, \sigma_{-.0.+}\right). \quad \text{(D5)}$$

These three estimates are obtained by (3) inverse interpolation interpolations:

$$A\emptyset_{-,0,+} = \mathbb{Z}^{-1}\left(A\emptyset^*, \sigma_{-,0,+}\right) \quad \text{(D6)}$$

which is feasible since (D5) is a one-one function over a suitably wide range of apparent agyrotropy and sigmas relevant to PIC and particle detectors in space (explicitly determined in Figure D2 below). In this way two values $A\emptyset_{\pm}$ that bracket the most consistent value of Vlasov agyrotropy $A\emptyset$ can be determined to associate with the $A\emptyset^*_{PIC}(N)$ determined directly from the pressure tensor using the methods of Appendix A. The reason for 3 estimates stems from the statistical character of (D2), there being no unique prediction for the floor of agyrotropy at a given N, just a highly likely range.

[53] Two dimensional, inverse interpolation via (D6) allows the determination of the fractional error F expected in the reconstructed Vlasov agyrotropy:

$$F = \frac{\text{Max}\{|A\emptyset_+ - A\emptyset_0|, |A\emptyset_- - A\emptyset_0|\}}{A\emptyset_0}$$

[54] This fraction is contoured in Figure D2 as a function of(σ_0, $A\emptyset^*$). The bounding red curve that rises to the right in the figure is the locus of conditions consistent with Vlasov gyrotropy. At large values of σ the bounding red curve makes an abrupt trend reversal, now possessing a negative slope. In this range the maximum value of $A\emptyset^*(\sigma_o)$ at these values of σ_o from equation (D1) is less than the assumed value of $A\emptyset^*$, making the inverse interpolation impossible. Accordingly, the region in this figure above and to the left of the cusped red curve is the domain where the original mapping is 1–1 and the reconstruction outlined here has a unique solution.

[55] The general pattern for F in the 1–1 domain is that it is smaller the further the observation is away from the vertical rising portion of the bounding red curve, with smallest values for largest $A\emptyset^*$ and smallest σ_0, where it can be as small as 10^{-7} rising to values near unity (green contour) as the observations approach the limiting, rising part of the red curve, where the unpacked Vlasov agyrotropy is zero. The fractional error rises as the rising red

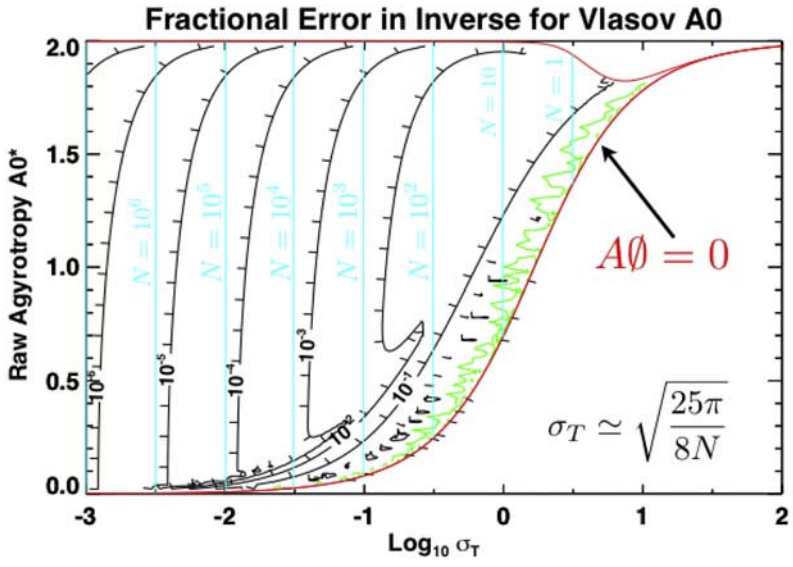

Figure D2. Illustrating typical regimes and errors for correcting the raw agyrotropy to the underlying agyrotropy of the Vlasov fluid being simulated.

bounding curve is approached and the precision of the reconstruction is going down; however at the same time the best estimate for Vlasov agyrotropy approaches zero at that red boundary, causing the absolute error to remain small in most quarters. It is this feature that allows the Harris sheet agyrotropy to be recovered in Figure B1. The vertical cyan lines in this figure reflect the operating point for a cell with the indicated number of particles involved in determining its moments. That number may be augmented as we have done here by time averaging or grid spatial averaging. When averaging over 3 output frames and a 7×7 grid our typical runs are operating at the $N_{eff} \simeq 66{,}000$, explaining how the recovered agyrotropy can have such small fractional errors (provided the grid averaging did not smooth out actual structure in the agyrotropy enroute).

[56] **Acknowledgments.** Discussions and manuscript comments by Homa Karamibadi are gratefully acknowledged. This work is based on work supported by the National Science Foundation under grant 0447423 and the Department of Energy grant DE-FC02-06ER54893 and NASA grant NNG05GC28G.

[57] Amitava Bhattacharjee thanks the reviewers for their assistance in evaluating this paper.

References

Bellan, P. M. (2006), *Fundamentals of Plasma Physics*, chap. 3, Cambridge Univ. Press, New York.

Bessho, N., and A. Bhattacharjee (2005), Collisionless reconnection in an electron-positron plasma, *Phys. Rev. Lett.*, *95*, 245001, doi:10.1103/PhysRevLett.95.245001.

Burlaga, L. F. (1995), *Interplanetary Magnetohydrodynamics*, Cambridge Univ. Press, New York.

Chacon, L., et al. (2007), Steady state properties of driven magnetic reconnection in 2D electron MHD, *Phys. Rev. Lett.*, *99*, 235001.

Daughton, W., and H. Karimabadi (2007), Collisionless magnetic reconnection in a large scale electron-positron plasma, *Phys. Plasma*, *14*, 072303, doi:10.1063/1.2749494.

Daughton, W., J. D. Scudder, and H. Karimabadi (2006), Full kinetic simulations of undriven magnetic reconnection with open boundary conditions, *Phys. Plasmas*, *13*, 072101, doi:10.1063/1.2218817.

Drake, J. F., M. Swisdak, M. Shay, B. N. Rogers, A. Zeiler, and C. Cattell (2002), Development of electron holes and anomalous resistivity in 3-D magnetic reconnection, 2002AGUFMSM51C.03D.

Golant, V. E., A. P. Zhilinsky, and I. E. Sakharov (1980), *Fundamentals of Plasma Physics*, 252 pp., Wiley Interscience, New York.

Harris, E. G. (1962), On a plasma sheath separating regions of oppositely directed magnetic field, *Nuovo Cim.*, *23*, 115–121, doi:10.1007/BF02733547.

Hasegawa, A. (1975), *Plasma Instabilities and Non-Linear Effects*, 83 pp., Springer, Berlin.

Hazeltine, R. D., and F. L. Waelbroeck (1998), *The Framework of Plasma Physics*, 14 pp., Perseus, Reading.

Henderson, P. D., C. J. Owen, A. D. Lahiff, I. V. Alexeev, A. N. Fazakerly, E. Lucek, and H. Reme (2006), Cluster PEACE observations of the electron pressure tensor divergence in the magnetotail, *Geophys. Res. Lett.*, *33*, L22106, doi:10.1029/2006GL027868.

Hesse, M., D. Winske, and M. Kuznetsova (1995), Hybrid modeling of collisionless reconnection in two-dimensional current sheets: Simulations, *J. Geophys. Res.*, *100*, 21,815, doi:10.1029/95JA01559.

Hesse, M., K. Schindler, J. Birn, and M. Kuznetsova (1999), The diffusion region in collisionless magnetic reconnection, *Phys. Plasma*, *6*, 1781.

Holdaway, R., J. Scudder, S. Li, and R. Glassberg (2008), False positive signatures of agyrotropy caused by gradients, *Eos Trans. AGU*, *88*(52), Fall Meet. Suppl., Abstract SH44A–1710.

Karimabadi, H., W. Daughton, and J. D. Scudder (2007), The multiscale structure of the electron diffusion region, *Geophys. Res. Lett.*, *34*, L13104, doi:10.1029/2007GL030306.

Kuznetsova, M., M. Hesse, and D. Winske (1998), Kinetic, quasi-viscous and bulk flow inertial effects in collisionless magnetic reconnection, *J. Geophys. Res.*, *103*, 199, doi:10.1029/97JA02699.

Lemaire, J., and L. F. Burlaga (1976), Diamagnetic boundary layers—A kinetic theory, *Astrophys. Space Sci.*, *45*, 303–325, doi:10.1007/BF00642667.

Mahajan, S. M., and R. D. Hazeltine (2000), Sheared-flow generalization of Harris sheet, *Phys. Plasma*, *7*(4), 1287.

Mozer, F. S. (2005), Criteria for and statistics of electron diffusion regions associated with sub solar magnetic field reconnection, *J. Geophys. Res.*, *110*, A12222, doi:10.1029/2005JA011258.

Parker, E. N. (1957), Newtonian development of the dynamic properties of ionized gases of low density, *Phys. Rev.*, *107*, 924–933, doi:10.1103/PhysRev.107.924.

Paschmann, G., B. U. O. Sonnerup, I. Papamasterakis, N. Sckopke, G. Haerendel, S. J. Bame, J. R. Asbridge, J. T. Gosling, C. T. Russell, and R. C. Elphic (1979), Plasma acceleration at the earth's magnetopause, evidence for reconnection, *Nature*, *282*, 243, doi:10.1038/282243a0.

Phan, T. D., G. Paschhmann, C. Twitty, F. S. Mozer, J. T. Gosling, J. P. Eastwood, M. Oieroset, H. Reme, and E. A. Lucek (2007), Evidence for magnetic reconnection initiated in the magnetosheath, *Geophys. Res. Lett.*, *34*, L14104, doi:10.1029/2007GL030343.

Pritchett, P. L. (2001), Geospace Modeling magnetic reconnection challenge: Simulation with a full particle electromagnetic code, *J. Geophys. Res.*, *106*, 3783, doi:10.1029/1999JA001006.

Ricci, P., J. U. Brackbill, W. Daughton, and G. Lapenta (2004), Influence of the lower hybrid drift instability on the onset of magnetic reconnection, *Phys. Plasmas*, *11*, 4102, doi:10.1063/1.1768552.

Rogers, B. N., R. E. Denton, J. F. Drake, and M. A. Shay (2001), Role of dispersive waves in collisionless reconnection, *Phys. Rev. Lett.*, *87*, 195004, doi:10.1103/PhysRevLett.87.195004.

Rossi, B., and S. Olbert (1970), *Introduction to the Physics of Space*, p. 121ff., McGraw-Hill, New York.

Scudder, J. D. (1997), Theoretical approaches to the description of magnetic merging: The need for finite β_e, anisotropic, ambipolar hall MHD, *Space Sci. Rev.*, *80*, 235–267, doi:10.1023/A:1004978021644.

Scudder, J. D., and F. S. Mozer (2005), Electron demagnetization and collisionless plasma in $\beta_e < 1$ plasmas, *Phys. Plasmas*, *12*, 092903, doi:10.1063/1.2046887.

Scudder, J. D., et al. (1995), Hydra—A 3-dimensional electron and ion hot plasma instrument for the polar spacecraft on the GGS mission, *Space Sci. Rev.*, *71*, 459–495, doi:10.1007/BF00751338.

Scudder, J. D., F. S. Mozer, N. C. Maynard, and C. T. Russell (2002), Fingerprints of collisionless reconnection at the separator: I. Ambipolar Hall signatures, *J. Geophys. Res.*, *107*(A10), 1294, doi:10.1029/2001JA000126.

Scudder, J. D., S. Li, W. Daughton, R. Holdaway, and R. Glassberg (2008), Direct detection of electron demagnetization and agyrotropy at electron diffusion regions, *Eos Trans. AGU*, *88*(52), Fall Meet. Suppl., Abstract SH43A–05.

Shay, M., J. Drake, B. Rogers, and R. Denton (2001), Alfvenic collisionless magnetic reconnection and the Hall term, *J. Geophys. Res.*, *106*, 3759.

Shay, M. A., J. F. Drake, and M. Swisdak (2007), Two scale structure of the electron dissipation region during collisionless magnetic reconnection, *Phys. Rev. Lett.*, *99*, 155002, doi:10.1103/PhysRevLett.99.155002.

Sonnerup, B. U. O., G. Paschmann, I. Papamastorakis, N. Sckopke, G. Haerendel, S. J. Bame, J. R. Asbridge, J. R. Gosling, and C. T. Russell (1981), Evidence for magnetic field reconnection at the earth's magnetopause, *J. Geophys. Res.*, *86*, 10049, doi:10.1029/JA086iA12p10049.

Vasyliunas, V. M. (1975), Theoretical models of magnetic field line merging, 1, *Rev. Geophys.*, *13*, 303–336, doi:10.1029/RG013i001p00303.

Walen, C. (1944), On the theory of sunspots, *Ark. Mat. Astron. Fys.*, *30A*, 15.

W. Daughton, Los Alamos National Laboratory, Los Alamos, NM 87545, USA.

J. Scudder, Department of Physics and Astronomy, University of Iowa, Iowa City, IA 52240, USA. (jack-scudder@uiowa.edu)